Dalton Transactions

PAPER

View Article Online
View Journal

Cite this: DOI: 10.1039/c8dt04408b

Lewis acid activated CO_2 reduction over a Ni modified Ni–Ge hydroxide driven by visible-infrared light†

Zhenyu Xin,‡[a] Lei Lu,‡[a] Bing Wang,[b] Xiaohui Wang,[a] Kai Zhu,*[c] Zhe Xu,[a] Zhentao Yu,[a] Shicheng Yan *[a] and Zhigang Zou[a,b]

Received 6th November 2018,
Accepted 4th December 2018

DOI: 10.1039/c8dt04408b

rsc.li/dalton

Improvement of light harvesting and reaction kinetics is of great importance for achieving efficient solar-driven CO_2 reduction. Here, a Ni modified low-crystalline Ni–Ge containing hydroxide with Lewis acid sites was synthesized in highly reductive $NaBH_4$ solution and exhibited 9.3 μmol $g_{cat.}^{-1}$ h^{-1} CO and 3.5 μmol $g_{cat.}^{-1}$ h^{-1} CH_4 generation rates under visible light irradiation, and even achieved a 3.8 μmol $g_{cat.}^{-1}$ h^{-1} CO evolution under infrared light irradiation. The wide-spectrum light harvesting resulted from the light absorption from the localized surface plasmonic resonance of Ni nanoparticles. In addition, the Lewis acid can activate C=O bonds to decrease the kinetic barriers of CO_2 reduction. The design concept that rationally combines the advantages of expanding the spectral response and activating CO_2 may offer a new strategy for efficient solar energy utilization.

Introduction

Photocatalytic CO_2 conversion into renewable solar fuels is a promising technique for solving energy shortage and global warming problems.[1] Generally, oxidation of H_2O into oxygen and reduction of CO_2 into carbon-based products (CO, CH_4 *etc.*), respectively, driven by photogenerated holes and electrons, are involved in this process. Both the half-reactions require high reaction energy and multi-electron consumption, thus resulting in slow reaction kinetics.[2] In addition to the kinetic limitations, the light harvesting of a photocatalyst is a thermodynamic limit for the maximum solar-to-chemical energy conversion efficiency. These facts indicate that decreasing kinetic barriers and increasing light harvesting are highly necessary for achieving an efficient CO_2 conversion.[3–6]

To decrease the kinetic barriers of the CO_2 reduction reaction, one of the most effective methods is to activate the reactants. Particularly, it has been well demonstrated that the CO_2 molecule can be activated by Lewis acids such as coordinately unsaturated metal ions, generally resulting from the fact that the lone pair electrons of each oxygen atom in CO_2 can be donated to the surface of Lewis acid centers.[7] Ti^{3+} as a Lewis acid on the anatase TiO_2 nanotubes allowed the creation of bent CO_2 structures, thus benefiting the dissociation of CO_2.[8] Similarly, in our previous work, Ge^{2+} on the α-Zn–Ge–O surface could effectively react with CO_2 to form carbon intermediate species (CO*), and even split CO_2 into C and O_2.[9] In addition, the oxygen vacancies (O_{Vs}) can serve as an electron mediator to facilitate the activation of molecules.[10–13] Accordingly, simultaneously activating CO_2 by a solid base and H_2O by O_{Vs} affords a two-fold enhancement in CO_2 reduction.[14] This evidence indicates that the activation of CO_2 and H_2O is indeed important for CO_2 conversion. However, there is a lack of methods to combine molecule activation with efficient light harvesting.

Herein, we aim to develop a strategy that simultaneously decreases the kinetic barriers of the reaction and expands the light harvesting. To confirm this purpose, a composite photocatalyst, a Ni modified low-crystalline Ni–Ge hydroxide with Lewis acid sites, was synthesized by an ion exchange reaction between $Ni(NO_3)_2$ and Na_2GeO_3 in sodium borohydride solution at 273 K. The coordinately unsaturated metal sites (Lewis acid sites) served as active sites for activating CO_2, and the localized surface plasmonic resonance (LSPR) effect of the Ni nanoparticles was used to broaden the optical absorption. A remarkable photocatalytic performance in CO_2 reduction was obtained under irradiation by visible and infrared light. We

[a]Jiangsu Key Laboratory of Artificial Functional Materials, Eco-materials and Renewable Energy Research Center (ERERC), National Laboratory of Solid State Microstructures, Collaborative Innovation Center of Advanced Microstructures, College of Engineering and Applied Sciences, Nanjing University, 210093, P. R. China. E-mail: yscfei@nju.edu.cn
[b]Jiangsu Province Key Laboratory for Nanotechnology, School of Physics, Nanjing University, Nanjing, Jiangsu 210093, P. R. China
[c]School of Information Science and Engineering, Nanjing University Jinling College, No. 8 Xuefu Road, Nanjing, Jiangsu 210089, P. R. China. E-mail: 25898099@qq.com

†Electronic supplementary information (ESI) available. See DOI: 10.1039/c8dt04408b

‡These authors contributed equally to this work.

have confirmed that the surface –OH as a solid proton on the low-crystalline Ni–Ge containing hydroxide could be easily oxidized by photogenerated holes to form H^+ and O_2 and recovered by H_2O, while the reduced $Ge^{\delta+}$ ($0 < \delta < 4$) as a Lewis acid is responsible for the activation of CO_2, significantly decreasing the reaction barriers. Our findings offer a simple route to introduce Lewis acids as active sites and the LSPR effect for effective utilization of visible-infrared light.

Experimental section

Synthesis of a Ni modified Ni–Ge containing hydroxide photocatalyst

To start with, Na_2GeO_3 powders were prepared by heating a stoichiometric mixture of GeO_2 and Na_2CO_3 at 1173 K for 12 h. After that, $NaBH_4$ powders (14 mM) were dissolved in the as-obtained Na_2GeO_3 aqueous solution (2 mM, 10 mL). The resulting mixed solution was then injected into $Ni(NO_3)_2$ aqueous solution (3 mM, 20 mL) with ice-water soaking. After magnetic stirring for 20 h in an ice bath, the resulting powders were collected by centrifugation, washing several times with deionized water, and freeze-drying for 48 h (denoted as Ni/$Ni_3Ge_2O_5(OH)_4$). For comparison, the same procedure without the addition of $NaBH_4$ was applied to synthesize a single-phase $Ni_3Ge_2O_5(OH)_4$.

Photocatalyst characterization

The crystallographic structure was identified by powder X-ray diffraction (XRD, Rigaku Ultima III, Japan, Cu Kα radiation) operating at 40 kV and 40 mA. The surface morphology and composition were analyzed using scanning electron microscopy (SEM, FEI Nova Nano SEM 230, USA). High-resolution images and selected area electron diffraction (SAED) patterns were obtained by transmission electron microscopy (TEM, FEI Tecnai G2 F30 S-Twin, USA) operating at 200 kV. Ultraviolet–visible (UV-vis) diffuse reflectance spectra (DRS) were recorded with a UV-vis spectrophotometer (UV-LAMBDA 950, PerkinElmer, USA) and were transformed into the absorption spectra according to the Kubelka–Munk relationship. Quantitative Fourier transform infrared spectroscopy (FT-IR) was performed using a Nicolet Nexus 870 infrared spectrometer (Nicolet, USA) under ambient conditions. Room-temperature steady-state photoluminescence (PL) spectroscopy and PL decay traces were obtained by using a fluorescence spectrofluorometer (HORIBA Fluorolog-3, HORIBA). The chemical state and valence band spectra of photocatalysts were investigated by X-ray photoelectron spectroscopy (XPS) on a PHI5000 Versa Probe (ULVAC-PHI, Japan) with monochromatized Al Kα X-ray radiation (1486.6 eV). The binding energy was determined by reference to the C 1s line at 284.6 eV. The elemental content (C_x) was determined by a formula $C_x = \frac{I_x/S_x}{\sum_i I_i/S_i}$, where I is the XPS peak area and S is the sensitivity factor. The specific surface area was measured by a nitrogen (N_2) adsorption–desorption technique using an automatic surface area analyzer (Micromeritics Tristar-3000, USA) after dehydration at 423 K for 3 h under N_2 flow. CO_2 adsorption was detected at 273 K based on the Brunauer–Emmett–Teller (BET) method at P/P_0 = 0.03. Mott–Schottky plots were determined using an electrochemical workstation (CHI Instruments CHI760E) at frequencies of 200, 500, and 1000 Hz in the dark.

Photocatalytic CO_2 reduction tests

The photocatalytic CO_2 reduction tests were conducted on a glass reactor by dispersing a photocatalyst (50 mg) onto a sample holder (area, 4.2 cm^2). The volume of the reaction system was about 230 mL. The light source was a 300 W Xe lamp and the radiation spectrum is shown in Fig. S1.† Before the irradiation, the reaction system was evacuated and flushed with CO_2 several times, and then high-purity CO_2 (99.999%) was introduced into the reaction chamber to achieve an ambient pressure. Subsequently, 0.4 mL of deionized water was injected into the chamber as a reductant, thus achieving a saturated vapor pressure (molar gas ratio of CO_2/H_2O was about 29 : 1). Prior to irradiation, the as-prepared photocatalyst was maintained in the dark for 12 h to reach the adsorption–desorption equilibrium of CO_2. The amount of O_2 from photocorrosion or CO_2 reduction was online determined using gas chromatography (GC-8A, MS-5A column, thermal conductivity detector, Ar carrier, Shimadzu, Japan). During the reaction, 1 mL gas was extracted by using a sampling needle from the chamber at given intervals for subsequent CO and CH_4 concentration analysis by gas chromatography (GC-2014, Shimadzu Corp., Japan).

Results and discussion

X-ray powder diffraction (XRD) analysis (Fig. 1a) showed that a mixture of Ni (JCPDS no. 04-0850) and $Ni_3Ge_2O_5(OH)_4$ (JCPDS no. 11-0097) was obtained by a reaction of $Ni(NO_3)_2$ and Na_2GeO_3 in $NaBH_4$ solution at 273 K (denoted as Ni/$Ni_3Ge_2O_5(OH)_4$). Single-phase $Ni_3Ge_2O_5(OH)_4$ crystals were obtained *via* a similar synthetic procedure without adding

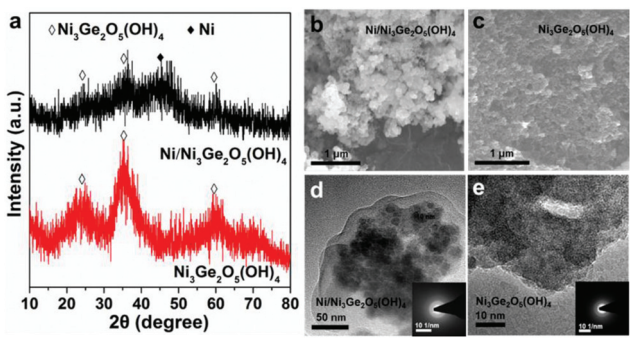

Fig. 1 (a) XRD patterns of Ni/$Ni_3Ge_2O_5(OH)_4$ and $Ni_3Ge_2O_5(OH)_4$. (b) The SEM image and (d) TEM image of Ni/$Ni_3Ge_2O_5(OH)_4$. The inset showed the SAED patterns of Ni/$Ni_3Ge_2O_5(OH)_4$. (c) The SEM image and (e) TEM image of $Ni_3Ge_2O_5(OH)_4$. The inset shows the SAED patterns of $Ni_3Ge_2O_5(OH)_4$.

$NaBH_4$ (Fig. 1a). No XRD peaks of Ni could be detected in a sample prepared by directly mixing the $NaBH_4$ solution and $Ni_3Ge_2O_5(OH)_4$ (Fig. S2†). However, the Ni nanoparticles could be obtained by $NaBH_4$ reduction of $Ni(NO_3)_2$. This evidence suggested that the formation of Ni in $Ni/Ni_3Ge_2O_5(OH)_4$ had the same crystallization process as the reduction of $Ni(NO_3)_2$ by $NaBH_4$. Energy dispersive spectroscopy (EDS) revealed that the atomic ratio of Ni : Ge in $Ni/Ni_3Ge_2O_5(OH)_4$ and $Ni_3Ge_2O_5(OH)_4$ was about 1.76 and 1.59, respectively (Fig. S3†). The higher Ni content in $Ni/Ni_3Ge_2O_5(OH)_4$ indicated the formation of Ni nanoparticles. Compared with $Ni_3Ge_2O_5(OH)_4$, the broadening of XRD peaks indicated a lower crystallinity of $Ni/Ni_3Ge_2O_5(OH)_4$. To further confirm that the low-crystallinity mixture was indeed composed of Ni and $Ni_3Ge_2O_5(OH)_4$, the as-prepared sample was heated at 673 K for 1 h under N_2 flow. The high-resolution transmission electron microscopy (HR-TEM) image of $Ni/Ni_3Ge_2O_5(OH)_4$ after annealing treatment showed two lattice spacings of 0.203 and 0.368 nm, which were assigned to the (111) facet of Ni and the (109) facet of $Ni_3Ge_2O_5(OH)_4$, respectively (Fig. S4†). In addition, HR-TEM observation showed that about 10 nm Ni nanoparticles clung to the $Ni_3Ge_2O_5(OH)_4$ particles (Fig. S4†), corresponding well with the size of Ni particles from $NaBH_4$ reduction of $Ni(NO_3)_2$ at 273 K (Fig. S5†).

The scanning electron microscopy (SEM) image showed that the $Ni/Ni_3Ge_2O_5(OH)_4$ sample presented an aggregation of irregular hundred-nanometre spherical particles (Fig. 1b). The morphology of the $Ni_3Ge_2O_5(OH)_4$ sample was similar to $Ni/Ni_3Ge_2O_5(OH)_4$ and exhibited a denser aggregation of irregular several-ten nanometer spherical particles (Fig. 1c). For $Ni/Ni_3Ge_2O_5(OH)_4$ and $Ni_3Ge_2O_5(OH)_4$, their low crystallinities were well confirmed by transmission electron microscopy (TEM) observation (Fig. 1d and e). Selected area electron diffraction (SAED) patterns revealed an obvious diffraction ring, suggesting that $Ni/Ni_3Ge_2O_5(OH)_4$ and $Ni_3Ge_2O_5(OH)_4$ were polycrystalline in nature.

Fig. 2a shows the UV-vis absorption spectra. As can be seen, the $Ni_3Ge_2O_5(OH)_4$ sample presented a strong UV absorption for a wavelength shorter than 320 nm. Other three absorption peaks at 350–500, 600–800 and after 900 nm were mainly attributed to the intermediate-band transition of Ni^{2+}.[15] For $Ni/Ni_3Ge_2O_5(OH)_4$, an extraordinary high absorption in the detected wavelength range was observed and overlapped with the absorption edge of $Ni_3Ge_2O_5(OH)_4$. As we know, Ni has a wide-spectrum range of localized surface plasmonic resonance (LSPR) that enhances the absorption ability and broadens the light response range.[16–18] Indeed, the as-prepared Ni nanoparticles by direct reduction of $Ni(NO_3)_2$ in $NaBH_4$ aqueous solution showed a strong light absorption in the wavelength range of 300–1500 nm (Fig. S6a†). And mixing the Ni and $Ni_3Ge_2O_5(OH)_4$ nanoparticles showed a similar UV-vis absorption spectrum to $Ni/Ni_3Ge_2O_5(OH)_4$ (Fig. S6b†), indicating that the expanding light absorption mainly originated from the LSPR effect of Ni nanoparticles. Extra light absorption could enhance the charge carrier production, thus improving the CO_2 reduction.

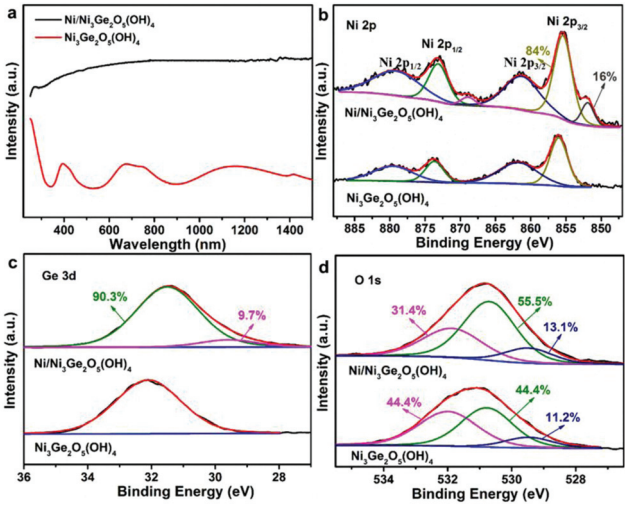

Fig. 2 (a) UV-vis absorption spectra of $Ni/Ni_3Ge_2O_5(OH)_4$ and $Ni_3Ge_2O_5(OH)_4$. (b) Ni 2p, (c) Ge 3d and (d) O 1s XPS spectra of $Ni/Ni_3Ge_2O_5(OH)_4$ and $Ni_3Ge_2O_5(OH)_4$.

The chemical environment of the elements was subsequently analysed by X-ray photoelectron spectroscopy (XPS). Fig. 2b shows that the Ni $2p_{3/2}$ XPS peaks of $Ni/Ni_3Ge_2O_5(OH)_4$ at 855.4 and 851.9 eV were respectively assigned to Ni^{2+} and Ni^0. According to the XPS peak area, the percentage composition of Ni^{2+} and Ni^0 was respectively calculated to be 84% and 16% in $Ni/Ni_3Ge_2O_5(OH)_4$. This suggested that the mole ratio of Ni/Ge in $Ni/Ni_3Ge_2O_5(OH)_4$ was about 1.78, which was in good agreement with the EDS result (Fig. S3†). The Ge^{4+} species was observed at 31.5 eV for $Ni/Ni_3Ge_2O_5(OH)_4$ and at 32.1 eV for $Ni_3Ge_2O_5(OH)_4$, respectively (Fig. 2c). About 0.6 eV lower binding energy was probably attributed to the lower crystallinity of $Ni/Ni_3Ge_2O_5(OH)_4$ compared to $Ni_3Ge_2O_5(OH)_4$, as demonstrated in XRD results. Indeed, a higher binding energy of Ge^{4+} (33.0 eV) was observed due to the high crystallinity of $Ni_3Ge_2O_5(OH)_4$ (Fig. S7†). In addition, the binding energy of reduced $Ge^{\delta+}$ in $Ni/Ni_3Ge_2O_5(OH)_4$ was observed at 29.6 eV, which was located between 31.5 eV of Ge^{4+} and 29.0 eV of Ge^0.[19] Quantitative analysis revealed that about 9.7% of the lattice Ge^{4+} was reduced to $Ge^{\delta+}$ during the formation of $Ni/Ni_3Ge_2O_5(OH)_4$.

During the crystallization of $Ni_3Ge_2O_5(OH)_4$, the Ge–O tetrahedral sheet and the Ni–OH octahedral sheet condensed to assemble the tetrahedral–octahedral structural layers, in which the hydroxyl in the octahedral sheet was partly substituted for the reactive oxygen atom in the tetrahedral sheet accompanied by the formation of Ge–O–Ni chemical bonds (Fig. S8†).[20,21] Therefore, the O 1s XPS could be deconvoluted into three peaks (Fig. 2d). Due to the bigger electronegativity of Ge (2.01) than Ni (1.91), the peaks at 529.5 and 530.8 eV were attributed to Ge–O–Ni and Ge–O bonds, respectively.[22] The O 1s XPS peak at 532.0 eV was assigned to the Ni–OH bonds.[23] Obviously, compared with $Ni_3Ge_2O_5(OH)_4$, the mole ratio of the Ge–O–Ni and Ge–O bonds on $Ni/Ni_3Ge_2O_5(OH)_4$ increased,

while the mole ratio of Ni–OH bonds decreased. This evidence indicated that the Ni–OH bonds were slightly unstable and the dehydroxylation may occur during the formation of Ni/$Ni_3Ge_2O_5(OH)_4$. The decreased amount of Ni–OH bonds would induce the increase in the relative mole ratio of Ge–O–Ni and Ge–O bonds, although the formation of $Ge^{\delta+}$ decreased the actual mole amount of the coordinated Ge–O bonds. The quantitative FT-IR spectrum analysis (Fig. S9†) revealed that the decreased vibrations of Ge–O (823 cm^{-1})[24] and Ni–OH bonds (3440 cm^{-1})[25] were both observed for Ni/$Ni_3Ge_2O_5(OH)_4$ compared with $Ni_3Ge_2O_5(OH)_4$. This fact further suggested that the reduced $Ge^{\delta+}$ species formed and the partial dehydroxylation occurred during the formation of Ni/$Ni_3Ge_2O_5(OH)_4$, probably due to the strong reduction ability of $NaBH_4$ solution.

The photocatalytic CO_2 reduction tests were carried out over the as-prepared Ni/$Ni_3Ge_2O_5(OH)_4$ and $Ni_3Ge_2O_5(OH)_4$ photocatalysts using H_2O as a reducing agent. Fig. 3 shows the typical time–course curves of CO and CH_4 yields. After full arc irradiation by a 300 W Xe lamp for 6 h, the CO and CH_4 yields (Fig. 3a and b) were 186.4 and 30.4 μmol $g_{cat.}^{-1}$ over Ni/$Ni_3Ge_2O_5(OH)_4$, respectively, about 3.1 and 6.3 times as much as those over $Ni_3Ge_2O_5(OH)_4$ (59.5 μmol $g_{cat.}^{-1}$ for CO and 4.8 μmol $g_{cat.}^{-1}$ for CH_4). Under a dark reaction or without a catalyst, no products could be detected. CO and CH_4 could only be detected under irradiation, and their yields increased while prolonging the irradiation time, proving that the CO_2 reduction was a light-driven catalytic reaction. In addition, only O_2 could be detected during vacuum irradiation for 6 h without CO_2 as a reactant, excluding the effect of possible organic residues on production detection (Table S1†).

The valence band edge of $Ni_3Ge_2O_5(OH)_4$ was determined by valence-band XPS to be 0.60 eV below the Fermi level by the linear extrapolation method (Fig. S10†). The Mott–Schottky plot (Fig. S11b†) suggested that $Ni_3Ge_2O_5(OH)_4$ was a p-type conducting semiconductor and the flat band potential was located at 1.70 V *vs.* normal hydrogen electrode (NHE, pH = 7). Therefore, the valence band edge (E_{VB}) of $Ni_3Ge_2O_5(OH)_4$ was 2.30 V *vs.* NHE, which was powerful enough to oxidize H_2O (0.82 V *vs.* NHE). Combined with the E_g value (3.88 eV) calculated by the UV-vis absorption edge, the conduction band edge (E_{CB}) for $Ni_3Ge_2O_5(OH)_4$ remained at about −1.58 V *vs.* NHE, was able to reduce CO_2 to form CO (−0.53 V *vs.* NHE) and CH_4 (−0.24 V *vs.* NHE). The E_{VB} and E_{CB} potentials of $Ni_3Ge_2O_5(OH)_4$ were thermodynamically enough to drive the CO_2 reduction to occur.

For Ni/$Ni_3Ge_2O_5(OH)_4$, the valence band edge was located at 0.22 eV below the Fermi level, whereas the valence band maximum energy blue-shifted toward the vacuum level at approximately −1.65 eV (Fig. S10†). During the formation of Ni/$Ni_3Ge_2O_5(OH)_4$, the strong reduction ability of $NaBH_4$ may induce surface disorder and hence produce the mid-gap states. The disorder-induced mid-gap states could upshift the valence band maximum energy of $Ni_3Ge_2O_5(OH)_4$, similar to the black TiO_2.[26,27] The Mott–Schottky plot (Fig. S11a†) suggested that the flat band potential of the Ni/$Ni_3Ge_2O_5(OH)_4$ composite was located at 1.55 V *vs.* NHE. Therefore, the E_{VB} of Ni/$Ni_3Ge_2O_5(OH)_4$ was 1.77 V *vs.* NHE. The E_{CB} of Ni/$Ni_3Ge_2O_5(OH)_4$ was expected to downshift due to the formation of $Ge^{\delta+}$, which would be demonstrated in the following photocatalytic CO_2 reduction tests under infrared light irradiation.

Brunauer–Emmett–Teller (BET) tests showed that the specific surface area for Ni/$Ni_3Ge_2O_5(OH)_4$ and $Ni_3Ge_2O_5(OH)_4$ was 16.15 and 33.26 m^2 $g_{cat.}^{-1}$, respectively (Fig. S12a†). The larger specific surface area resulted from the smaller particle size of $Ni_3Ge_2O_5(OH)_4$ than Ni/$Ni_3Ge_2O_5(OH)_4$. The CO_2 adsorbed amount of Ni/$Ni_3Ge_2O_5(OH)_4$ (3.65 mg $g_{cat.}^{-1}$) was obviously lower than that of $Ni_3Ge_2O_5(OH)_4$ (8.41 mg $g_{cat.}^{-1}$) (Fig. S12b†). The amount of CO_2 adsorbed was normalized by the specific surface area to be 0.25 mg m^{-2} for $Ni_3Ge_2O_5(OH)_4$, which was much close to 0.23 mg m^{-2} for Ni/$Ni_3Ge_2O_5(OH)_4$. This evidence revealed that the CO_2 adsorbed capacity was not the main factor that contributed to the higher CO_2 reduction efficiency over Ni/$Ni_3Ge_2O_5(OH)_4$.

To check the effect of light absorption on CO_2 reduction, the CO_2 reduction tests were carried out under visible light (λ > 420 nm). As given in Fig. 3c and d, under visible light irradiation, both Ni/$Ni_3Ge_2O_5(OH)_4$ and $Ni_3Ge_2O_5(OH)_4$ samples showed continuously increased CO and CH_4 yields while increasing the irradiation time. After irradiation for 6 h, the CO and CH_4 yields were 55.9 and 20.8 μmol $g_{cat.}^{-1}$ for Ni/$Ni_3Ge_2O_5(OH)_4$, about 17 and 25 times higher than those for $Ni_3Ge_2O_5(OH)_4$ (3.1 μmol $g_{cat.}^{-1}$ CO and 0.8 μmol $g_{cat.}^{-1}$ CH_4). The low CO and CH_4 yields over $Ni_3Ge_2O_5(OH)_4$ were probably attributed to the weak visible light absorption *via* interband transition of Ni^{2+}, as demonstrated by the UV-vis result. Similarly, an inter-band transition in the defective WO_{3-x} is able to drive CO_2 reduction under infrared light irradiation.[28] In addition, steady-state photoluminescence spectra showed that $Ni_3Ge_2O_5(OH)_4$ exhibited 640 and 770 nm emission peaks under the excitation of 470 nm (Fig. S13†), which could be

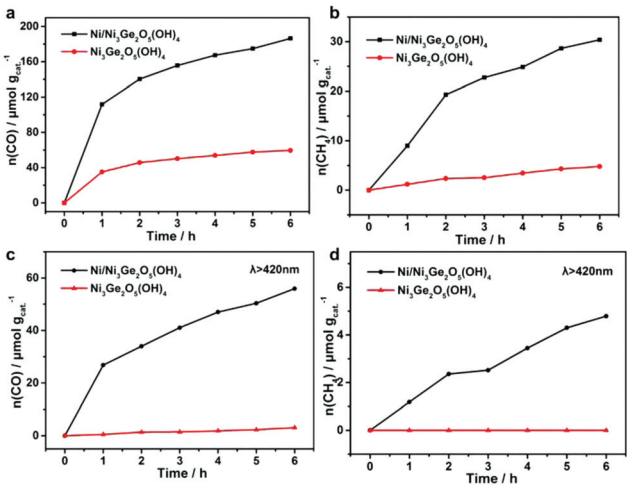

Fig. 3 CO and CH_4 yields for Ni/$Ni_3Ge_2O_5(OH)_4$ and $Ni_3Ge_2O_5(OH)_4$ under full arc (a and b) and visible light irradiation (c and d) for 6 h.

ascribed to the recombination from the intermediate band to the valence band.[29] For $Ni/Ni_3Ge_2O_5(OH)_4$, the broadening emission peak from 620 to 850 nm centered at 750 nm would correspond to the recombination of abundant defects (Fig. S13†).[30] The decreased PL intensity for $Ni/Ni_3Ge_2O_5(OH)_4$ *versus* $Ni_3Ge_2O_5(OH)_4$ could be ascribed to the effective suppression of radiative charge recombination. Additionally, the average fluorescence lifetimes of $Ni/Ni_3Ge_2O_5(OH)_4$ and $Ni_3Ge_2O_5(OH)_4$ were 4.75 ns and 3.40 ns respectively (Fig. S13†), suggesting the improvement of the efficiency of charge transport.

In our case, the infrared light response (λ > 800 nm) of $Ni_3Ge_2O_5(OH)_4$ is not able to drive the CO_2 reduction reaction. However, $Ni/Ni_3Ge_2O_5(OH)_4$ still produced 22.5 μmol $g_{cat.}^{-1}$ CO and 0.9 μmol $g_{cat.}^{-1}$ CH_4 after infrared irradiation for 6 h (Fig. S14†). This fact indicated that the carbon-based product formation was probably driven by the hot electrons from the plasma effect of Ni particles. The possible channel of electron transfer for photocatalysis under infrared irradiation was that the LSPR excited electrons in plasmonic metal transferred to the conduction band or mid-gap states of $Ni/Ni_3Ge_2O_5(OH)_4$ and subsequently took part in the CO_2 reduction reaction.[26] With the modification of Ni, the resulting hot electrons increased the charge concentration, thus improving the CO_2 reduction reaction rates. However, no products could be detected over the physically mixed Ni + $Ni_3Ge_2O_5(OH)_4$ sample under infrared light irradiation. This evidence meant that $Ni/Ni_3Ge_2O_5(OH)_4$ was able to drive the half-reaction of water oxidation under infrared light irradiation thermodynamically. As a result, the total CO_2 reduction efficiency over $Ni/Ni_3Ge_2O_5(OH)_4$ under visible light irradiation was even higher than that over $Ni_3Ge_2O_5(OH)_4$ under full arc irradiation. The energy of infrared light (λ > 800 nm) was lower than 1.55 eV, while the location of the Fermi level of Ni metal was 0.65 V *vs.* NHE. Thus, the E_{CB} for $Ni/Ni_3Ge_2O_5(OH)_4$ was expected to be downshifted below −0.9 V (NHE), possibly resulting from the formation of reduced $Ge^{\delta+}$ species. Similar Ge^{2+} inducing E_{CB} downshift was observed in amorphous α-Zn–Ge–O.[9] Indeed, the formation of CO and CH_4 under infrared light irradiation would indicate that the LSPR effect of Ni on $Ni/Ni_3Ge_2O_5(OH)_4$ was energetically enough for driving the CO_2 reduction reaction to occur, as described in Fig. 4.

XPS results had confirmed that the coordinately unsaturated $Ge^{\delta+}$, a typical Lewis acid, formed on the $Ni/Ni_3Ge_2O_5(OH)_4$. Evidently, after 6 h CO_2 reduction reaction, the content of $Ge^{\delta+}$ further increased and the amount of Ge–O bonds decreased (Fig. 5a and b). The increased amount of $Ge^{\delta+}$ would originate from photogenerated electrons to reduce Ge^{4+}, as demonstrated in our previous work.[9] Indeed, the vacuum irradiation of $Ni/Ni_3Ge_2O_5(OH)_4$ for 6 h induced about 16.1% increase in the content of $Ge^{\delta+}$ species (Fig. 5c and d). The binding energy of Ge^{4+} decreased from 31.5 to 31.2 eV, proving that the coordination environment of surface Ge^{4+} changed and the element Ge tended to gain electrons under irradiation. In addition, no obvious signal of Ni^{+} as unsaturated metal sites was detected possibly due to the instability of

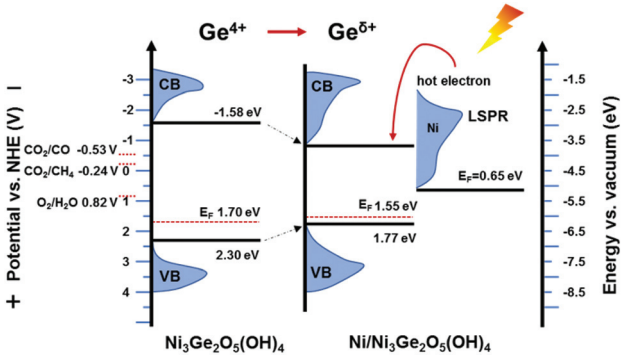

Fig. 4 Schematic energy band diagram for solar CO_2 overall splitting into CO and CH_4.

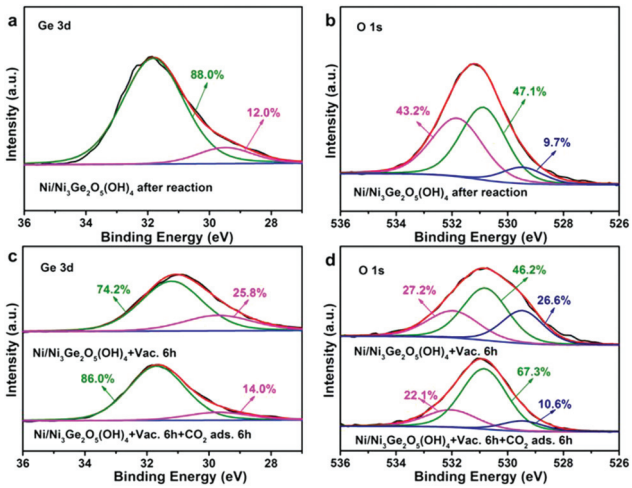

Fig. 5 (a) Ge 3d and (b) O 1s XPS spectra of $Ni/Ni_3Ge_2O_5(OH)_4$ after reaction. (c) Ge 3d and (d) O 1s XPS spectra of $Ni/Ni_3Ge_2O_5(OH)_4$ after vacuum irradiation for 6 h (denoted as $Ni/Ni_3Ge_2O_5(OH)_4$ + Vac.6 h) and of $Ni/Ni_3Ge_2O_5(OH)_4$ + Vac.6 h after CO_2 adsorption for 6 h (denoted as $Ni/Ni_3Ge_2O_5(OH)_4$ + Vac.6 h + CO_2 ads.6 h).

Ni^{+} (Fig. S15†).[31] Therefore, the activation of the CO_2 molecule during photocatalysis was mainly related to the Ge element. However, no obvious change in Ge 3d XPS spectra and Ni 2p XPS spectra for $Ni_3Ge_2O_5(OH)_4$ before and after vacuum irradiation was observed (Fig. S16 and S17†), further confirming that the formation of coordinately unsaturated metal sites was related to the low crystallinity of $Ni/Ni_3Ge_2O_5(OH)_4$.

Generally, the coordinately unsaturated $Ge^{\delta+}$ could serve as active sites to interact with O of CO_2. To check the activation role of $Ge^{\delta+}$, CO_2 adsorption under dark conditions was carried out after vacuum irradiation of $Ni/Ni_3Ge_2O_5(OH)_4$. Obviously, the quantitative FT-IR analysis indicated that the intensity of two bands at 1390 and 1560 cm^{-1} (Fig. 6a), respectively, corresponding to the symmetric and asymmetric stretching vibrations of O=C–O^{-},[32,33] both increased after the CO_2 adsorption under dark conditions. Meanwhile, the increased intensity of the Ge–O band at 823 cm^{-1} could be ascribed to

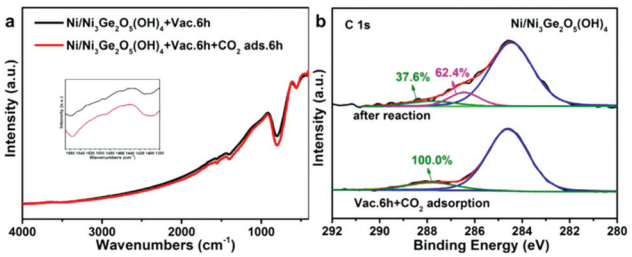

Fig. 6 (a) FT-IR spectra of $Ni/Ni_3Ge_2O_5(OH)_4$ + Vac.6 h and $Ni/Ni_3Ge_2O_5(OH)_4$ + Vac.6 h + CO_2 ads.6 h. (b) C 1s XPS spectra of $Ni/Ni_3Ge_2O_5(OH)_4$ after reaction and $Ni/Ni_3Ge_2O_5(OH)_4$ + Vac.6 h + CO_2 ads.6 h. The inset in (a) showed the enlarged FT-IR spectra for $Ni/Ni_3Ge_2O_5(OH)_4$.

the interactions of $Ge^{\delta+}$ and CO_2. After CO_2 adsorption, the O 1s XPS spectra of $Ni/Ni_3Ge_2O_5(OH)_4$ with vacuum irradiation showed that the content of Ge–O at 530.8 eV increased (Fig. 5d). Simultaneously, the Ge 3d XPS spectra demonstrated that the binding energy of Ge^{4+} increased from 31.2 to 31.7 eV for $Ni/Ni_3Ge_2O_5(OH)_4$ with pre-irradiation under vacuum before and after CO_2 adsorption, suggesting that the Ge tended to lose electrons due to a strong interaction between CO_2 and $Ge^{\delta+}$ (Fig. 5c). Obviously, electron transfer between unsaturated $Ge^{\delta+}$ and CO_2 occurred.

The peak at 287.8 eV of the C 1s XPS spectrum for CO_2 adsorbed $Ni/Ni_3Ge_2O_5(OH)_4$ with pre-irradiation under vacuum was attributed to the C=O bonds (Fig. 6b),[34] indicative of the formation of C=O species. During the CO_2 reduction reaction, the C 1s XPS spectrum could be deconvoluted into three peaks: 287.8 eV for C=O bonds, 286.4 eV for C–O bonds,[35] and 284.6 eV for adventitious standard reference carbon (Fig. 6b). The content of C=O bonds at 287.8 eV decreased and that of C–O bonds at 286.4 eV appeared. This fact meant that CO_2 was activated to the C=O species *via* a strong interaction between O of CO_2 and $Ge^{\delta+}$ on $Ni/Ni_3Ge_2O_5(OH)_4$. Subsequently, C=O species were converted into C–O species *via* the assistance of photoelectrons, which may serve as an important intermediate for the formation of CO and CH_4. For $Ni_3Ge_2O_5(OH)_4$ without $Ge^{\delta+}$, the content of Ge–O observed from the Ge XPS spectra (Fig. S16†) and the FT-IR spectra (Fig. S18†) remained unchanged after CO_2 adsorption for 6 h, further confirming the activation effect of $Ge^{\delta+}$.

The O_2 generated from photocorrosion under vacuum for 1 h was 1472 μmol $g_{cat.}^{-1}$ for $Ni/Ni_3Ge_2O_5(OH)_4$ and 37 μmol $g_{cat.}^{-1}$ for $Ni_3Ge_2O_5(OH)_4$ (Table S1†), respectively. This fact indicated that the low-crystalline $Ni/Ni_3Ge_2O_5(OH)_4$ was prone to be photocorroded due to its weak constraint of the crystal lattice. Under a CO_2 atmosphere, after visible light irradiation for 1 h the O_2 yield was 897 μmol $g_{cat.}^{-1}$ for $Ni/Ni_3Ge_2O_5(OH)_4$ and 14 μmol $g_{cat.}^{-1}$ for $Ni_3Ge_2O_5(OH)_4$, respectively. Obviously, the lower O_2 generation rate resulted from the interactions between CO_2 and Lewis acid sites. The quantitative FT-IR analysis (Fig. 6a) and related O 1s XPS spectra (Fig. 5d) of $Ni/Ni_3Ge_2O_5(OH)_4$ after vacuum irradiation showed that the Ni–OH species decreased obviously, indicating that Ni–OH could be consumed by the photogenerated holes. In other words, the lattice Ni–OH could serve as a proton source. After the H_2O adsorption (Fig. S19†), the FT-IR peak intensity of Ni–OH recovered, suggesting that the –OH can be regenerated by H_2O. The O 1s XPS spectrum (Fig. 5b) and the FT-IR spectrum (Fig. S20a†) of $Ni/Ni_3Ge_2O_5(OH)_4$ after reaction showed that the content of Ni–OH found no obvious drop-off after the photocatalytic reaction, further confirming the regeneration of Ni–OH during the reaction. For $Ni_3Ge_2O_5(OH)_4$, the Ni–OH species slightly involved with the photocatalytic CO_2 reduction, as confirmed by the consistent analysis of O 1s XPS spectra (Fig. S16b and S16d†) and FT-IR spectra (Fig. S20b†).

Considering that Ni–OH on $Ni/Ni_3Ge_2O_5(OH)_4$ could be consumed by photogenerated holes, the CO_2 photoreduction tests were performed under full arc irradiation under high-purity CO_2 in the absence of H_2O. Both CO and CH_4 were detected under irradiation, confirming that Ni–OH could serve as the proton source for CO_2 reduction. In the absence of H_2O, the CO and CH_4 yields over $Ni/Ni_3Ge_2O_5(OH)_4$ were 343.2 and 51.7 μmol $g_{cat.}^{-1}$ after irradiation for 6 h (Fig. 7), which were 1.8 times and 1.7 times as much as those over $Ni/Ni_3Ge_2O_5(OH)_4$ with the addition of H_2O. The CO_2 reduction efficiency abnormally increased without the addition of H_2O as the reactant. Under the coexistence of CO_2 and H_2O, competitive molecule adsorption would occur during the reduction reaction of CO_2 by H_2O. The H_2O molecule, which is a strongly polar molecule, would exhibit a stronger interaction with $Ge^{\delta+}$ compared to the quadrupole CO_2 molecule.[14,36] Therefore, $Ge^{\delta+}$ tended to activate H_2O, resulting in a higher proton releasing, while in turn the activation of CO_2 was limited, thus causing low CO and CH_4 yields over $Ni/Ni_3Ge_2O_5(OH)_4$ with the addition of H_2O. Similarly, $Ni/Ni_3Ge_2O_5(OH)_4$ + Vac.6 h showed lower CO and CH_4 yields than those of $Ni/Ni_3Ge_2O_5(OH)_4$ (Fig. 7) due to the limitation of proton releasing. CO_2 reduction without the addition of H_2O showing

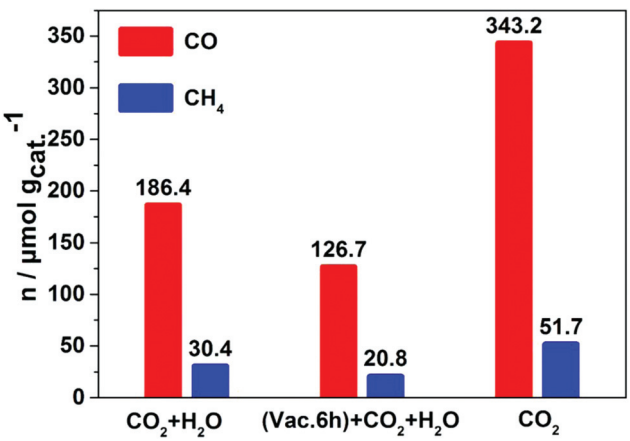

Fig. 7 CO (red line) and CH_4 (blue line) yields for $Ni/Ni_3Ge_2O_5(OH)_4$, $Ni/Ni_3Ge_2O_5(OH)_4$ + Vac.6 h and $Ni/Ni_3Ge_2O_5(OH)_4$ without H_2O as reactants under full arc light irradiation for 6 h.

higher CO and CH_4 yields over $Ni/Ni_3GeO_5(OH)_4$ was ascribed to the more matching reaction rates.

As a conclusion, proton releasing and CO_2 activation were equally vital for CO_2 photocatalytic reduction. $Ge^{\delta+}$ as a Lewis acid activating chemically inert CO_2 and Ni as a plasmonic promoter enhancing the light absorption improved CO_2 reduction performance over $Ni/Ni_3Ge_2O_5(OH)_4$. Surface Ni–OH as a proton source offered a new path to release protons for CO_2 reduction. The above experimental results allow us to give deeper insights into the lattice hydroxyl assisted photocatalytic CO_2 reduction and the effect of Ni NPs on photocatalytic performance.

The possible reaction mechanism for enhanced reduction efficiency of CO_2 over $Ni/Ni_3Ge_2O_5(OH)_4$ to CO and CH_4 under irradiation is shown as follows:

$$Ni/Ni_3Ge_2O_5(OH)_4 + \text{light} \rightarrow h^+ + e^- \quad (1)$$

$$4h^+ + 4Ni - OH^- \rightarrow 4H^+ + O_2 + 2Ni - O^{2-} \quad \text{or} \quad 4h^+ + 2H_2O \rightarrow 4H^+ + O_2 \quad (2)$$

$$Ge^{4+} + (4-\delta)\, e^- \rightarrow Ge^{\delta+} \quad (3)$$

$$(4-\delta)\, CO_2 + Ge^{\delta+} \rightarrow (4-\delta)\, CO_2^- + Ge^{4+} \quad (4)$$

$$CO_2^- + e^- + 2H^+ \rightarrow CO + H_2O \quad \text{or} \quad CO_2^- + 7e^- + 8H^+ \rightarrow CH_4 + 2H_2O \quad (5)$$

$$2H_2O + 2Ni\text{–}O^{2-} \rightarrow 4Ni\text{–}OH^- \quad (6)$$

From the above mechanism, photogenerated electrons to reduce Ge^{4+} to form $Ge^{\delta+}$ as a Lewis acid and photogenerated holes to oxidize Ni–OH can occur under light irradiation. The abundant $Ge^{\delta+}$ as a Lewis acid is energetically favorable for the adsorption of CO_2 into C═O species. Ni–OH is used as another proton source and is regenerated by H_2O. The CO_2 activation and –OH utilization as a proton source can effectively accelerate this light-driven reaction and achieve excellent photocatalytic performance. In addition, the LSPR of Ni over the photocatalyst enables the use of visible light and infrared light to improve the solar-to-chemical conversion. Therefore, the design concept for $Ni/Ni_3Ge_2O_5(OH)_4$, which is easy to introduce $Ge^{\delta+}$ and possesses adequate –OH and LSPR properties, provides a novel pathway to enhance photocatalytic activity.

Conclusions

In summary, the low crystalline hydroxide plasmonic photocatalyst with a weak lattice constraint for oxygen atoms is rationally prepared as a highly efficient catalyst for visible light or infrared light CO_2 reduction. The LSPR of metallic Ni tremendously expands the range of spectral response. $Ge^{\delta+}$ activates C═O bonds to decrease the energy barriers of CO_2 reduction. The surface lattice hydroxyl is not only joint with the formation of $Ge^{\delta+}$ but also simultaneously acting as a proton source for CO_2 reduction to divert the path of proton releasing from kinetically sluggish water oxidation. Consequently, the low crystalline $Ni/Ni_3Ge_2O_5(OH)_4$ exhibits remarkable visible-light and infrared-light photocatalytic performance especially compared with $Ni_3Ge_2O_5(OH)_4$. The design concept of simultaneously activating CO_2, promoting proton releasing and expanding the range of spectral response can be a new strategy for efficient solar energy utilization. This work might encourage the study on composite material design to establish the coupling of different modifications of materials.

Conflicts of interest

There are no conflicts to declare.

Acknowledgements

This work was supported primarily by the National Basic Research Program of China (2013CB632404), the National Natural Science Foundation of China (51872135, 51572121, 21603098, and 21633004), the Natural Science Foundation of Jiangsu Province (BK20151265, BK20151383, and BK20150580), the program B for outstanding PhD candidate of Nanjing University (201702B084), the Postdoctoral Science Foundation of China (2017M611784) and the Fundamental Research Funds for the Central Universities (021314380133 and 021314380084).

References

1 K. Li, X. An, K. Park, M. Khraisheh and J. Tang, *Catal. Today*, 2014, **224**, 3–12.
2 W. Tu, Y. Zhou and Z. Zou, *Adv. Mater.*, 2014, **26**, 4607–4626.
3 S. Wang, S. Yan, X. Ma and J. Gong, *Energy Environ. Sci.*, 2011, **4**, 3805–3819.
4 O. Bikondoa, C. Pang, R. Ithnin, C. Muryn, H. Onishi and G. Thornton, *Nat. Mater.*, 2006, **5**, 189–192.
5 I. Thomann, B. Pinaud, Z. Chen, B. Clemens, T. Jaramillo and M. Brongersma, *Nano Lett.*, 2011, **11**, 3440–3446.
6 T. Woolerton, S. Sheard, E. Reisner, E. Pierce, S. Ragsdale and F. Armstrong, *J. Am. Chem. Soc.*, 2010, **132**, 2132–2133.
7 V. Indrakanti, D. Kubicki and H. Schobert, *Energy Environ. Sci.*, 2009, **2**, 745–758.
8 G. Ramesha, J. Brennecke and P. Kamat, *ACS Catal.*, 2014, **4**, 3249–3254.
9 B. Wang, X. Wang, L. Lu, C. Zhou, Z. Xin, J. Wang, X. Ke, G. Sheng, S. Yan and Z. Zou, *ACS Catal.*, 2017, **8**, 516–525.
10 H. Kristoffersen, J. Hansen, U. Martinez, Y. Wei, J. Matthiesen, R. Streber, R. Bechstein, E. Lægsgaard, F. Besenbacher, B. Hammer and S. Wendt, *Phys. Rev. Lett.*, 2013, **110**, 146101.
11 J. Ding, Z. Dai, F. Qin, H. Zhao, S. Zhao and R. Chen, *Appl. Catal., B*, 2017, **205**, 281–291.

12 H. Li, J. Shang, Z. Ai and L. Zhang, *J. Am. Chem. Soc.*, 2015, **137**, 6393–6399.
13 H. Li, J. Shang, H. Zhu, Z. Yang, Z. Ai and L. Zhang, *ACS Catal.*, 2016, **6**, 8276–8285.
14 L. Lu, B. Wang, S. Wang, Z. Shi, S. Yan and Z. Zou, *Adv. Funct. Mater.*, 2017, **27**, 1702447.
15 N. Kuleshov, V. Shcherbitsky, V. Mikhailov, S. Kück, J. Koetke, K. Petermann and G. Huber, *J. Lumin.*, 1997, **71**, 265.
16 X. Meng, T. Wang, L. Liu, S. Ouyang, P. Li, H. Hu, T. Kako, H. Iwai, A. Tanaka and J. Ye, *Angew. Chem., Int. Ed.*, 2014, **126**, 11662.
17 Z. Xiong, X. Chen, X. Wang, L. Peng, D. Yan, H. Lei, Y. Fu, J. Wu, Z. Li, X. An and W. Wu, *Appl. Surf. Sci.*, 2013, **268**, 524.
18 H. Liu, T. Dao, L. Liu, X. Meng, T. Nagao and J. Ye, *Appl. Catal., B*, 2017, **209**, 183.
19 R. Shalvoy, G. Fisher and P. Stiles, *Phys. Rev. B: Solid State*, 1977, **15**, 1680.
20 A. Krasilin and E. Khrapova, *Russ. J. Appl. Chem.*, 2017, **90**, 22.
21 Y. Yang, Q. Liang, J. Li, Y. Zhuang, Y. He, B. Bai and X. Wang, *Nano Res.*, 2011, **4**, 882.
22 K. Li and D. Xue, *J. Phys. Chem. A*, 2006, **110**, 11332.
23 I. Casella, M. Guascito and M. Sannazzaro, *J. Electroanal. Chem.*, 1999, **462**, 202.
24 S. Rivillon, Y. Chabal, F. Amy and A. Kahn, *Appl. Phys. Lett.*, 2005, **87**, 253101.
25 S. Yang, X. Wu, C. Chen, H. Dong, W. Hu and X. Wang, *Chem. Commun.*, 2012, **48**, 2773.
26 X. Chen, L. Liu, Y. Peter and S. Mao, *Science*, 2011, **331**, 746–750.
27 L. Shi, Z. Li, T. Dao, T. Nagao and Y. Yang, *J. Mater. Chem. A*, 2018, **6**, 12978–12984.
28 L. Liang, X. Li, Y. Sun, Y. Tan, X. Jiao, H. Ju, Z. Qi, J. Zhu and Y. Xie, *Joule*, 2018, **2**, 1004.
29 C. Yang, M. Qin, Y. Wang, D. Wan, F. Huang and J. Lin, *Sci. Rep.*, 2013, **3**, 1286.
30 L. Ye, K. Deng, F. Xu, L. Tian, T. Peng and L. Zan, *Phys. Chem. Chem. Phys.*, 2012, **14**, 82–85.
31 L. Van Robbroeck, E. Goovaerts and D. Schoemaker, *Phys. Status Solidi B*, 1985, **132**, 179–187.
32 V. Nadtochenko, A. Rincon, S. Stanca and J. Kiwi, *J. Photochem. Photobiol., A*, 2005, **169**, 131.
33 K. Ogura, M. Kobayashi, M. Nakayama and Y. Miho, *J. Electroanal. Chem.*, 1998, **449**, 101.
34 Y. Wu, P. Wang, X. Zhu, Q. Zhang, Z. Wang, Y. Liu, G. Zou, Y. Dai, M. Whangbo and B. Huang, *Adv. Mater.*, 2018, **30**, 1704342.
35 J. Hou, H. Cheng, O. Takeda and H. Zhu, *Angew. Chem., Int. Ed.*, 2015, **127**, 8600.
36 F. Brandani and D. Ruthven, *Ind. Eng. Chem. Res.*, 2004, **43**, 8339.

